Supplement of Atmos. Chem. Phys., 26, 3417–3438, 2026
https://doi.org/10.5194/acp-26-3417-2026-supplement

Atmospheric Chemistry and Physics
Open Access

Supplement of

Sub-seasonal and spatial variations in ozone formation and co-control potential for secondary aerosols in the Guanzhong basin, central China

Ruonan Wang et al.

Correspondence to: Ningning Zhang (zhangnn@ieecas.cn)

SI. Model description and configuration

The WRF-Chem model (Grell et al., 2005), which has been further modified by Li et al. (2010; 2011a; 2011b; 2012), is employed in the present study. This specific version of the model has been successfully used to examine the widespread particulate and O_3 pollution in China within recent years (Li et al., 2017a; Wu et al., 2019; Le et al., 2020; Wu et al., 2020). To be brief, the Community Multi-scale Air Quality (CMAQ) aerosol module (AERO5) developed by the US EPA is used for aerosol prediction (Binkowski and Roselle, 2003). For gas-phase simulating, the SAPRC-99 mechanism (Statewide Air Pollution Research Centre, version 1999) is incorporated into the model. Inorganic aerosols are predicted based on a thermodynamic model: the ISORROPIA Version 1.7 (Nenes et al., 1998). The secondary organic aerosol (SOA) is calculated using a non-traditional SOA module containing volatility basis set (VBS) modeling approach as well as glyoxal and methylglyoxal contributions (Li et al., 2011b). The Fast Tropospheric Ultraviolet and Visible (FTUV) radiation module is used to calculate the gas-phase species photolysis rates with aerosol and cloud effects on photochemistry (Tie et al., 2003; Li et al., 2005). The wet deposition follows the method in the CMAQ module, and the surface dry deposition of chemical species is based on Wesely (1989), which improves the calculation of bulk surface resistances along three mass transfer pathways. The anthropogenic emission inventory utilized in the model is MEIC (Multi-resolution Emission Inventory for China), which encompasses industrial, agricultural, residential, transportation, and power generation contributions and is developed by Li et al. (2017) and Zheng et al. (2018) and further adjusted to 2022 according to observations. Biogenic emissions in the WRF-Chem model are online calculated by the Model of Emissions of Gases and Aerosols from Nature (MEGAN) Version 2.04 (Guenther et al., 2006). Table S1 provides the model details.

S2. Statistical methods for validation

Statistical parameters comprising the mean bias (MB), root mean square error (RMSE), and the index of agreement (IOA) are applied to validating the model performance of air pollutants simulations.

$$\mathrm{MB} = \frac{1}{\mathrm{N}}\sum_{\mathrm{i}=1}^{\mathrm{N}}(\mathrm{P_i} - \mathrm{O_i})$$

$$\mathrm{RMSE} = \left[\frac{1}{\mathrm{N}}\sum_{\mathrm{i}=1}^{\mathrm{N}}(\mathrm{P_i} - \mathrm{O_i})^2\right]^{\frac{1}{2}}$$

$$\mathrm{IOA} = 1 - \frac{\sum_{\mathrm{i}=1}^{\mathrm{N}}(\mathrm{P_i}-\mathrm{O_i})^2}{\sum_{\mathrm{i}=1}^{\mathrm{N}}(|\mathrm{P_i}-\bar{\mathrm{O}}|+|\mathrm{O_i}-\bar{\mathrm{O}}|)^2}$$

Where N is the number of simulations utilized for evaluation. $\mathrm{P_i}$ and $\mathrm{O_i}$ represents the predicted and observed pollutant concentrations, respectively. $\bar{\mathrm{O}}$ denotes the average observations. The MB of zero indicates

that model over-predictions and under-predictions exactly cancel each other. For IOA, the value of 0 insinuates that there is no relationship; while the IOA of 1 implies a perfect agreement between the observations and simulations.

S3. Model validation

Considering the key role of meteorological conditions in air pollution simulations, Figure S2 displays diurnal profiles of the simulated and observed 2-m air temperature, relative humidity, 10-m wind speed and direction at Jinghe meteorological site from May to August in 2022. The WRF-Chem model reproduces successfully the temporal variations of the temperature, with the IOA valuing 0.99, but slightly overestimates the temperature against observations, with the MB of 0.04 ºC. The model also performs well in tracking the temporal variations of the near-surface RH, with the IOA of 0.95. However, the model is subject to underestimating the RH, with the MB of -1.80%. The model reasonably simulates temporal variations of the near-surface wind speed and directions compared to observations, with the IOA of 0.70 and 0.87, respectively.

Figure S3 provides the predicted and observed horizontal distributions of $PM_{2.5}$, O_3, NO_2 and SO_2 concentrations against the simulated wind fields during warm season (from May to August) of 2022 in the GZB. In eastern GZB, the northeasterly wind is prevailing, causing transboundary transport of air pollutants from outside of the GZB. In middle and western GZB, the wind is weak or disordered generally due to blocking of mountains, which is favorable for accumulation of air pollutants. In southern, the prevailing of southerly winds could bring BVOCs emissions from the abundant forests in the Qinling mountains, which chemically react with anthropogenic emissions in the basin and contribute to the pollution. The simulated $PM_{2.5}$ and O_3 concentrations are spatially consistent well with the observations, with high levels in the eastern and central basin and relatively low concentrations in the western basin. The model well captures the horizontal distribution of SO_2 and NO_2 concentrations, which concentrate in urban cores due to their point emissions. Figure S4 depicts the temporal variations of simulated and observed near-surface $PM_{2.5}$, O_3, NO_2, SO_2 and CO concentrations averaged over monitoring sites in the GZB from May to August 2022. The model underestimates $PM_{2.5}$ and NO_2 concentrations, with MBs of -0.2 μg m^{-3} and -0.4 μg m^{-3}, respectively. O_3 concentrations are slightly overestimated, with MB of 0.1 μg m^{-3}. IOAs of all pollutants range of 0.52-0.72, indicating that the model generally well captures their temporal profiles.

Generally, the simulated criteria pollutant concentrations are generally in good agreement with observations,

indicating that the WRF-Chem model is capable of representing major physical and chemical processes and well produces the temporal variations associated with synoptic conditions.

SI References

Binkowski, F. S. and Roselle, S. J.: Models-3 Community Multiscale Air Quality (CMAQ) model aerosol component 1: Model description, J. Geophys. Res., 108, D6, doi:10.1029/2001JD001409, 2003.

Chen, F. and Dudhia, J.: Coupling an advanced land surface–hydrology model with the Penn State–NCAR MM5 modeling system. Part I: Model implementation and sensitivity, Mon. Weather Rev., 129, 569–585, doi:10.1175/1520-0493(2001)129<0569:CAALSH>2.0.CO;2, 2001.

Chou, M. D. and Suarez, M. J.: A solar radiation parameterization for atmospheric studies, NASA Tech. Memo. 104606, 15 pp., 1999.

Chou, M. D., Suarez, M. J., Liang, X. Z., Yan, M. H., and Cote, C.: A thermal infrared radiation parameterization for atmospheric studies, NASA Tech. Memo. 104606, 19 pp., 2001.

Grell, G. A. and Devenyi, D.: A generalized approach to parameterizing convection combining ensemble and data assimilation techniques, Geophys. Res. Lett., 29, 1693, doi:10.1029/2002GL015311, 2002.

Grell, G. A., Peckham, S. E., Schmitz, R., McKeen, S. A., Frost, G., Skamarock, W. C., and Eder, B.: Fully coupled "online" chemistry within the WRF model, Atmos. Environ., 39, 6957–6975, doi:10.1016/j.atmosenv.2005.04.027, 2005.

Guenther, A., Karl, T., Harley, P., Wiedinmyer, C., Palmer, P. I., and Geron, C.: Estimates of global terrestrial isoprene emissions using MEGAN (Model of Emissions of Gases and Aerosols from Nature), Atmos. Chem. Phys., 6, 3181–3210, doi:10.5194/acp-6-3181-2006, 2006.

Hong, S.-Y. and Lim, J.-O. J.: The WRF single-moment 6-class microphysics scheme (WSM6), Asia-Pac. J. Atmos. Sci., 42, 129–151, 2006.

Horowitz, L. W., Walters, S., Mauzerall, D. L., Emmons, L. K., Rasch, P. J., Granier, C., Tie, X. X., Lamarque, J. F., Schultz, M. G., Tyndall, G. S., Orlando, J. J., and Brasseur, G. P.: A global simulation of tropospheric ozone and related tracers: Description and evaluation of MOZART, version 2, J. Geophys. Res., 108, 4784, doi:10.1029/2002JD002853, 2003.

Janjić, Z. I.: Nonsingular implementation of the Mellor–Yamada level 2.5 scheme in the NCEP meso model, NCEP Office Note 436, 61 pp., 2002.

Le, T. H., Wang, Y., Liu, L., Yang, J. N., Yung, Y. L., Li, G. H., and Seinfeld, J. H.: Unexpected air pollution with marked emission reductions during the COVID-19 outbreak in China, Science, 369, 702–706, doi:10.1126/science.abb7431, 2020.

Li, G., Bei, N., Cao, J., Wu, J., Long, X., Feng, T., Dai, W., Liu, S., Zhang, Q., and Tie, X.: Widespread and persistent ozone pollution in eastern China during the non-winter season of 2015: observations and source attributions, Atmos. Chem. Phys., 17, 2759–2774, doi:10.5194/acp-17-2759-2017, 2017.

Li, G., Zhang, R., Fan, J., and Tie, X.: Impacts of black carbon aerosol on photolysis and ozone, J. Geophys. Res., 110, D23206, doi:10.1029/2005JD005898, 2005.

Li, M., Liu, H., Geng, G. N., Hong, C. P., Liu, F., Song, Y., Tong, D., Zheng, B., Cui, H. Y., Man, H. Y., Zhang, Q., and He, K. B.: Anthropogenic emission inventories in China: a review, Natl. Sci. Rev., 4, 834–866, doi:10.1093/nsr/nwx150, 2017.

Nenes, A., Pandis, S. N., and Pilinis, C.: ISORROPIA: A new thermodynamic equilibrium model for multiphase multicomponent inorganic aerosols, Aquat. Geochem., 4, 123–152, doi:10.1007/s10498-997-3776-7, 1998.

Tie, X., Madronich, S., Walters, S., Zhang, R., Rasch, P., and Collins, W.: Effect of clouds on photolysis and oxidants in the troposphere, J. Geophys. Res., 108, 4642, doi:10.1029/2003JD003659, 2003.

Wesely, M. L.: Parameterization of surface resistances to gaseous dry deposition in regional-scale numerical models, Atmos. Environ., 23, 1293–1304, doi:10.1016/0004-6981(89)90153-4, 1989.

Wu, J., Bei, N., Hu, B., Liu, S., Wang, Y., Shen, Z., Li, X., Liu, L., Wang, R., Liu, Z., Cao, J., Tie, X., Molina, L. T., and Li, G.: Aerosol–photolysis interaction reduces particulate matter during wintertime haze events, Proc. Natl. Acad. Sci. USA, 117, 9755–9761, doi:10.1073/pnas.1919728117, 2020.

Wu, J., Bei, N., Hu, B., Liu, S., Zhou, M., Wang, Q., Li, X., Liu, L., Feng, T., Liu, Z., Wang, Y., Cao, J., Tie, X., Wang, J., Molina, L. T., and Li, G.: Is water vapor a key player of the wintertime haze in North China Plain?, Atmos. Chem. Phys., 19, 8721–8739, doi:10.5194/acp-19-8721-2019, 2019.

Zheng, B., Tong, D., Li, M., Liu, F., Hong, C., Geng, G., Li, H., Li, X., Peng, L., Qi, J., Yan, L., Zhang, Y., Zhao, H., Zheng, Y., He, K., and Zhang, Q.: Trends in China's anthropogenic emissions since 2010 as the consequence of clean air actions, Atmos. Chem. Phys., 18, 14095–14111, doi:10.5194/acp-18-14095-2018, 2018.

Table S1: WRF-Chem model configurations.

Region	**Guanzhong Basin (GZB)**
Simulation period	From 01May to 31 August, 2022
Domain size	150×150
Domain center	34.25°N, 109°E
Horizontal resolution	6 km × 6 km
Vertical resolution	35 vertical levels with a stretched vertical grid with spacing ranging from 30m near the surface to 500m at 2.5 km and 1 km above 14 km
Microphysics scheme	WRF Single-Moment six-class graupel scheme (Hong and Lim, 2006)
Boundary layer scheme	Mellor–Yamada–Janjic turbulent kinetic energy scheme (Janjic, 2002)
Surface layer scheme	MYJ surface scheme (Janjic, 2002)
Land-surface scheme	Unified Noah land-surface model (Chen and Dudhia, 2001)
Longwave radiation scheme	Goddard longwave scheme (Chou and Suarez, 2001)
Shortwave radiation scheme	Goddard shortwave scheme (Chou and Suarez, 1999)
Meteorological boundary and initial conditions	NCEP 1°×1°reanalysis data
Chemical initial and boundary conditions	WACCM 6-h output
Anthropogenic emission inventory	SAPRC-99 chemical mechanism emissions with the base year of 2017. (Li et al., 2017; Zheng et al., 2018)
Biogenic emission inventory	MEGAN model developed by Guenther et al. (2006)

Table S2: Monthly number of MDA8 O_3 exceedance days during the warm-season in the GZB from 2014 to 2024.

Days	2014	2015	2016	2017	2018	2019	2020	2021	2022	2023	2024
May	0	0	2	4	3	2	3	3	3	2	11
June	0	1	12	12	17	11	4	10	13	10	10
July	0	1	8	16	3	7	6	7	8	11	3
August	0	1	2	10	10	4	1	4	3	3	10

Table S3：The monthly FNR derived from satellite retrievals averaged in the GZB during warm-seasons from 2021 to 2023.

FNR	May	June	July	August
2021	0.90	1.19	1.20	1.61
2022	0.91	1.31	1.50	1.77
2023	0.97	1.20	1.43	1.51

Table S4: Emission ratio of monthly anthropogenic NO_X to VOCs and their sector contributions in the GZB during the warm season in 2022.

	May		June		July		August	
Emission Ratio (NO_X / AVOCs)	0.34		0.31		0.27		0.30	
	NO_X	AVOCs	NO_X	AVOCs	NO_X	AVOCs	NO_X	AVOCs
*Industry (%)	28.84	24.58	22.82	25.74	66.43	69.34	68.90	68.48
*Power plants (%)	37.31	35.44	34.58	34.09	0.85	0.92	0.84	0.82
*Transport (%)	24.94	33.16	35.94	32.34	15.85	14.81	15.20	14.30
*Residential (%)	8.90	6.82	6.65	7.82	16.87	14.93	15.05	16.41

* denotes the individual's contribution to total emissions from source emissions.

Table S5: Monthly mean concentrations of NO_X (ppb), $HO\cdot$ (ppt) and $HO_2\cdot$ (ppt) in the areas of the GZB and five cities during the warm season in 2022.

	May			June			July			August		
	NO_X	$HO\cdot$	$HO_2\cdot$	NO_X	$HO\cdot$	$HO_2\cdot$	NO_X	$HO\cdot$	$HO_2\cdot$	NO_X	$HO\cdot$	$HO_2\cdot$
GZB	18.09	0.23	6.32	14.69	0.32	15.23	12.47	0.35	18.62	11.44	0.3	18.66
XA	18.9	0.22	7.25	14.22	0.31	17.72	11.35	0.34	21.36	11.08	0.29	20.62
XY	14.85	0.25	6.59	10.07	0.36	18.89	8.1	0.39	22.61	7.23	0.31	23.34
WN	33.2	0.16	2.45	32.8	0.24	4.94	29.64	0.24	5.62	24.08	0.26	8.05
TC	11.83	0.27	4.68	9.05	0.38	11.6	6.62	0.43	16.95	7.45	0.35	16.06
BJ	10.95	0.26	6.7	10.04	0.35	12.59	9.7	0.4	16.52	9.45	0.32	16.14

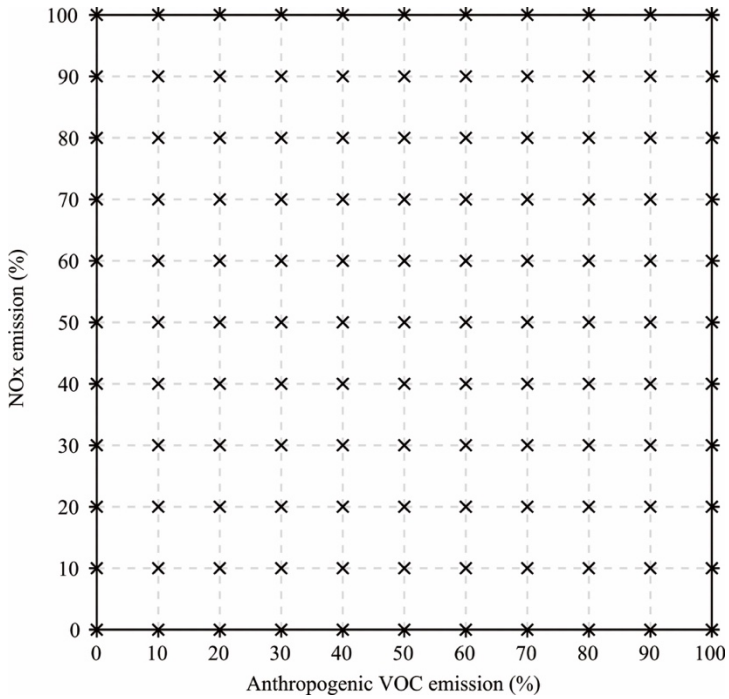

Figure S1: Emission reduction matrix of NO_X and VOCs for O_3 sensitivity study. The crosses represent 121 scenarios with different combinations of NO_X and AVOC emission reductions.

5

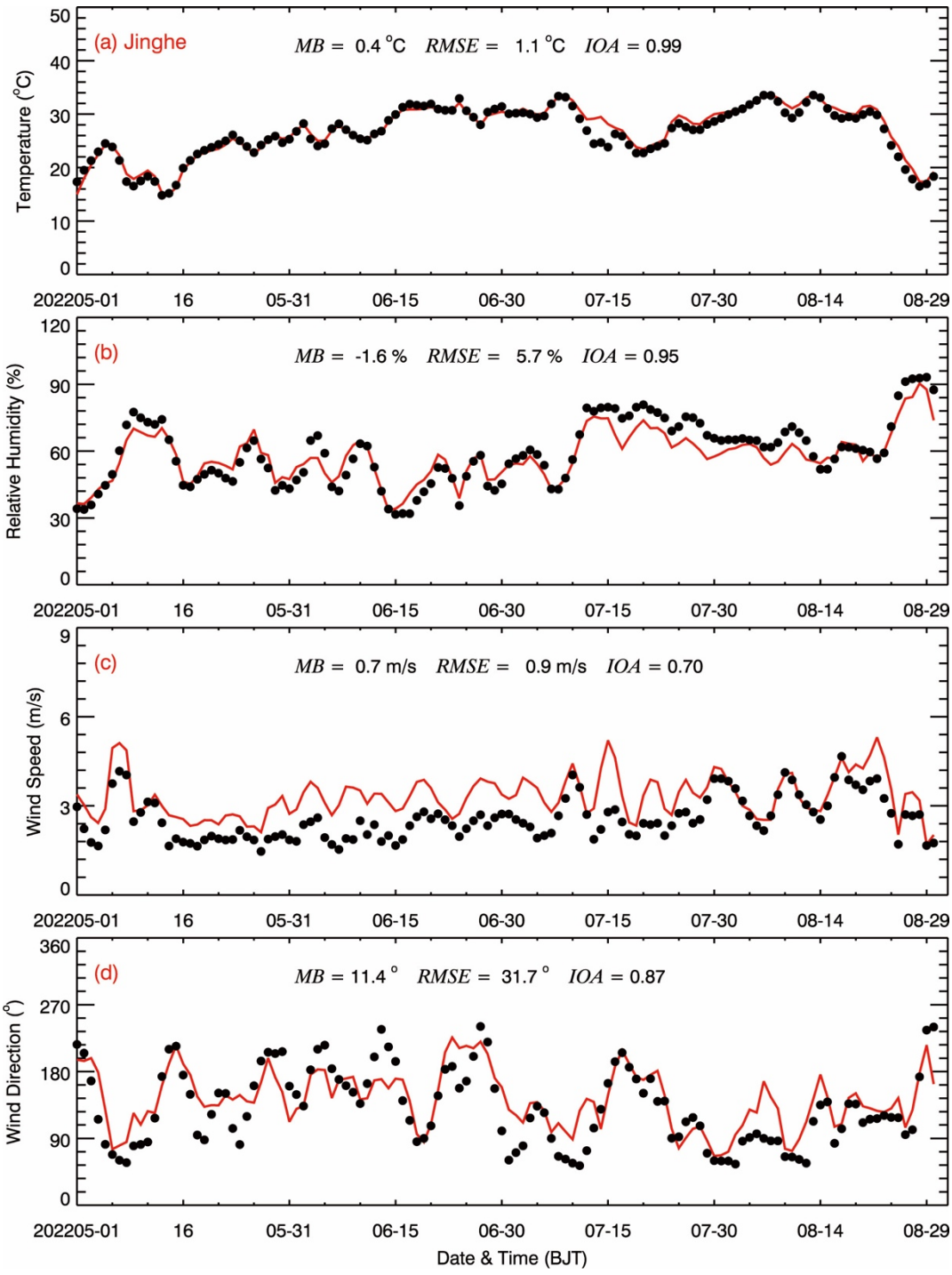

Figure S2: Temporal variations of predicted (red) and observed (black) (a) temperature at 2 m, (b) relative humid at 2 m, (c) wind speed and (d) wind direction at 10 m at Jinghe meteorological monitoring site from May to August 2022. The model performance statistic metrics of MB, RMSE and IOA are also shown.

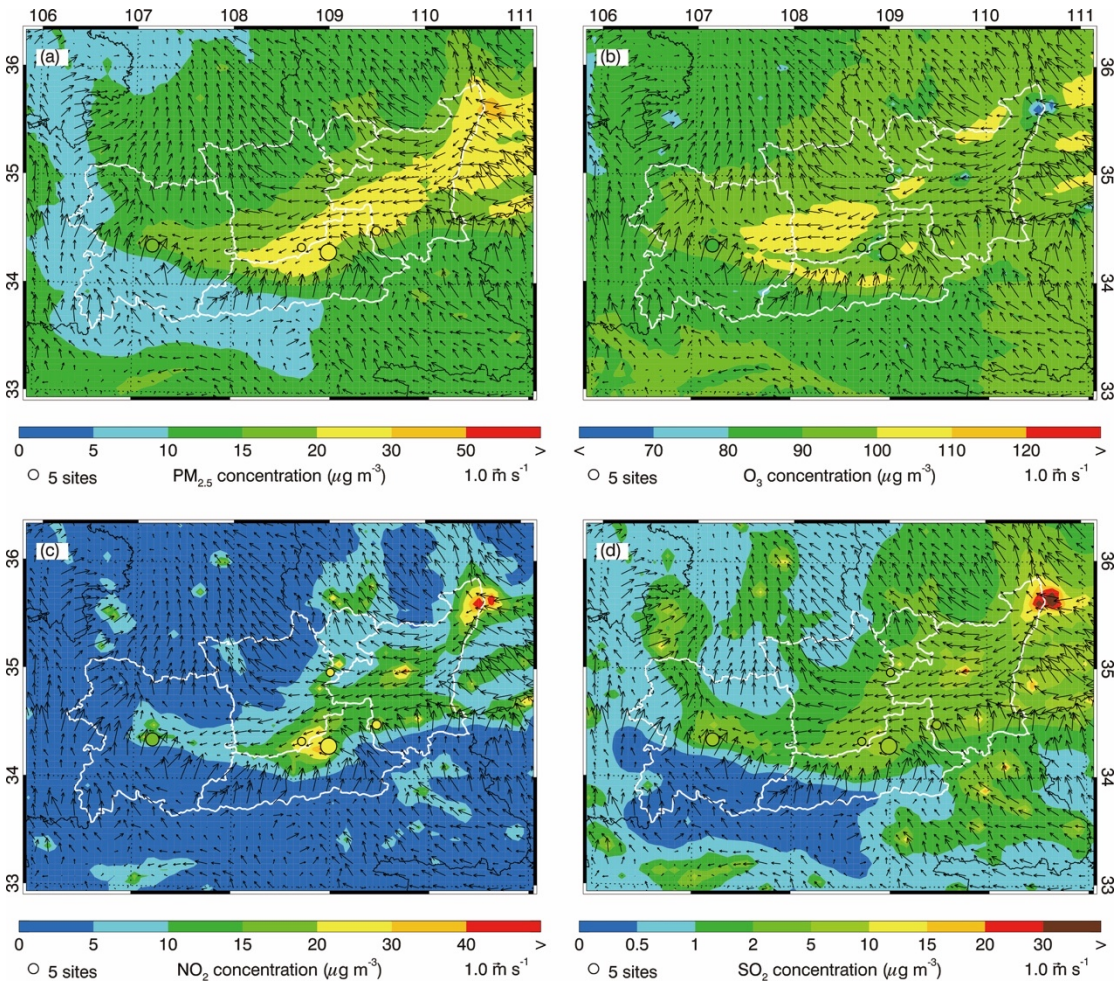

Figure S3: Pattern comparisons of simulated versus observed average (a) $PM_{2.5}$, (b) O_3, (c) NO_2, and (d) SO_2 concentrations from May to August 2022. Colored circles: observations; color contour: simulations; black arrows: simulated near-surface winds.

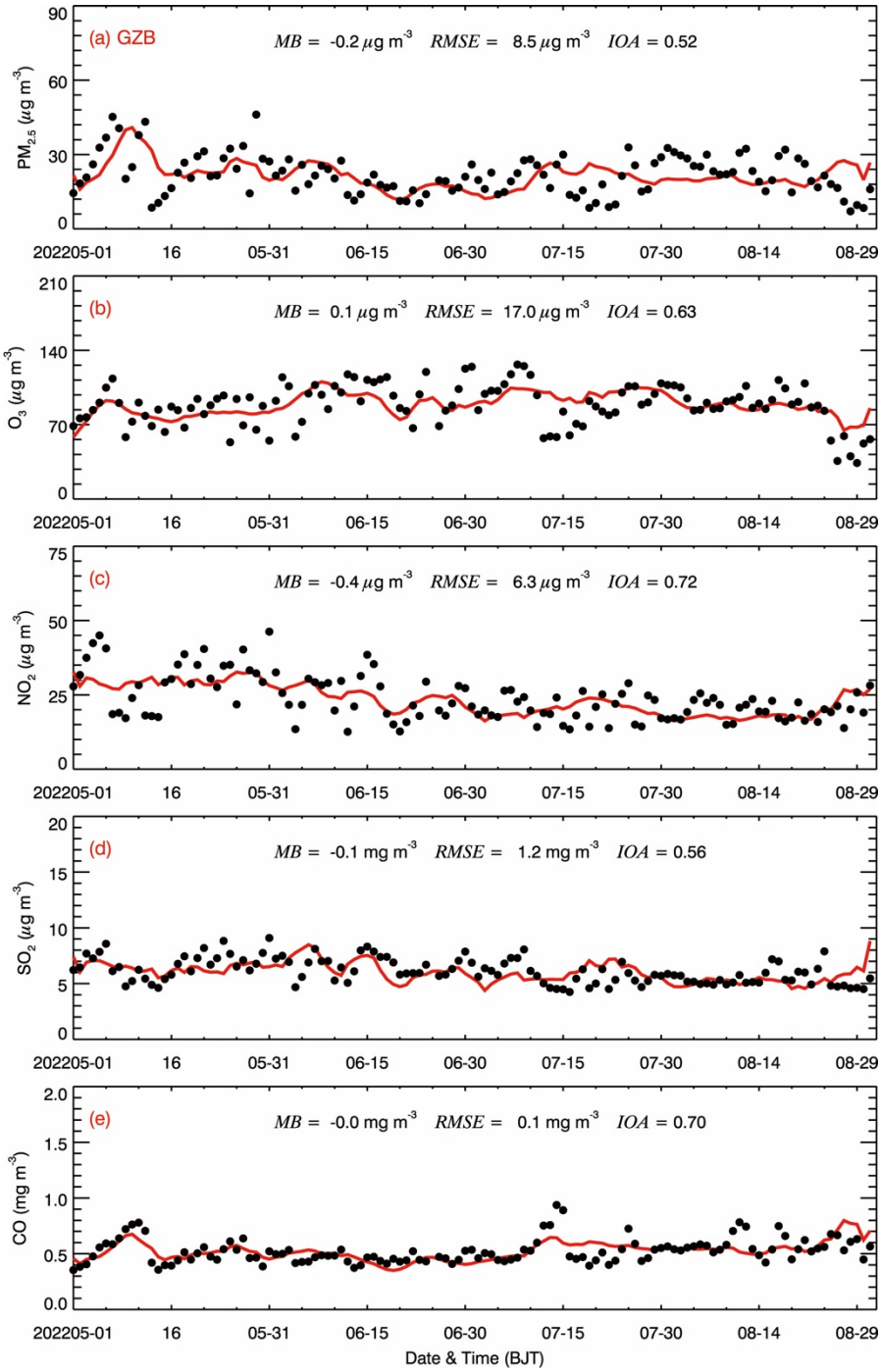

Figure S4: Diurnal profiles of measured (black dots) and predicted (red line) (a) $PM_{2.5}$, (b) O_3, (c) NO_2, (d) SO_2, and (e) CO concentrations averaged over all ambient monitoring stations in the GZB from May to August 2022.

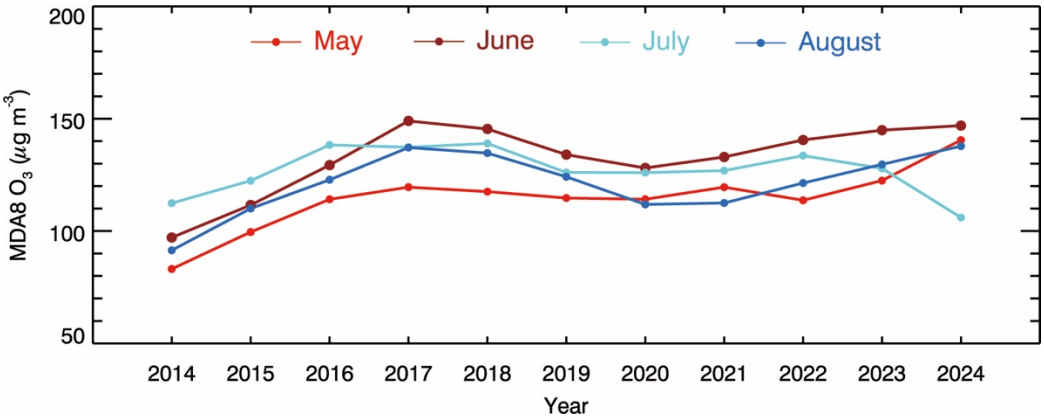

Figure S5: Interannual variations of monthly mean observed MDA8 O_3 concentrations in the GZB during warm-seasons of 2014–2024.

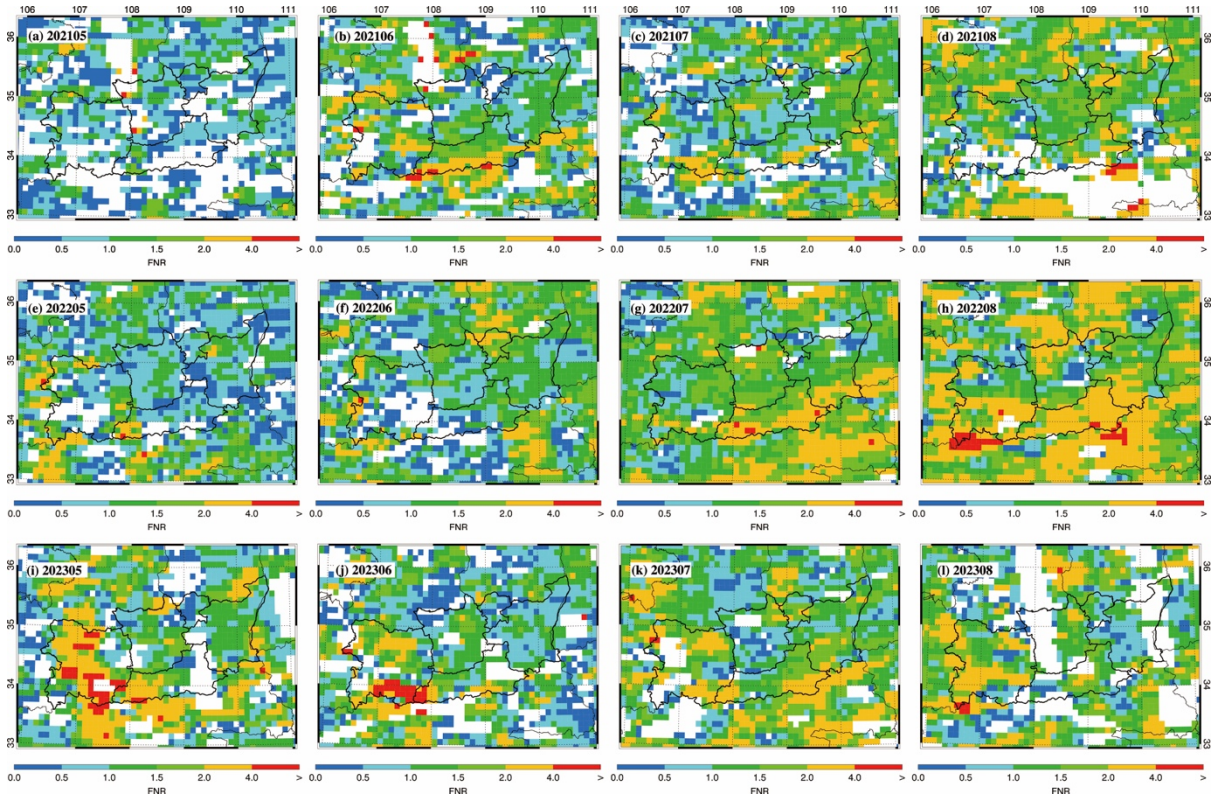

Figure S6: Spatial distribution of the satellite-derived formaldehyde-to-NO_2 ratio (FNR) over the GZB and surrounding regions. Monthly mean FNR values for the warm seasons (May–August) of (a–d) 2021, (e–h) 2022, and (i–l) 2023 are shown. FNR is calculated from tropospheric column densities of HCHO and NO_2 retrieved by the OMI sensor. According to typical threshold ranges applied in China, FNR values below 1.0 (blue tones) generally indicate VOCs-limited ozone formation regimes, values between 1.0 and 2.0 (green-yellow tones) indicate transitional regimes, and values above 2.0 (orange-red tones) indicate NO_X-limited regimes. Data gaps (white areas) are primarily due to cloud cover affecting the satellite retrievals.

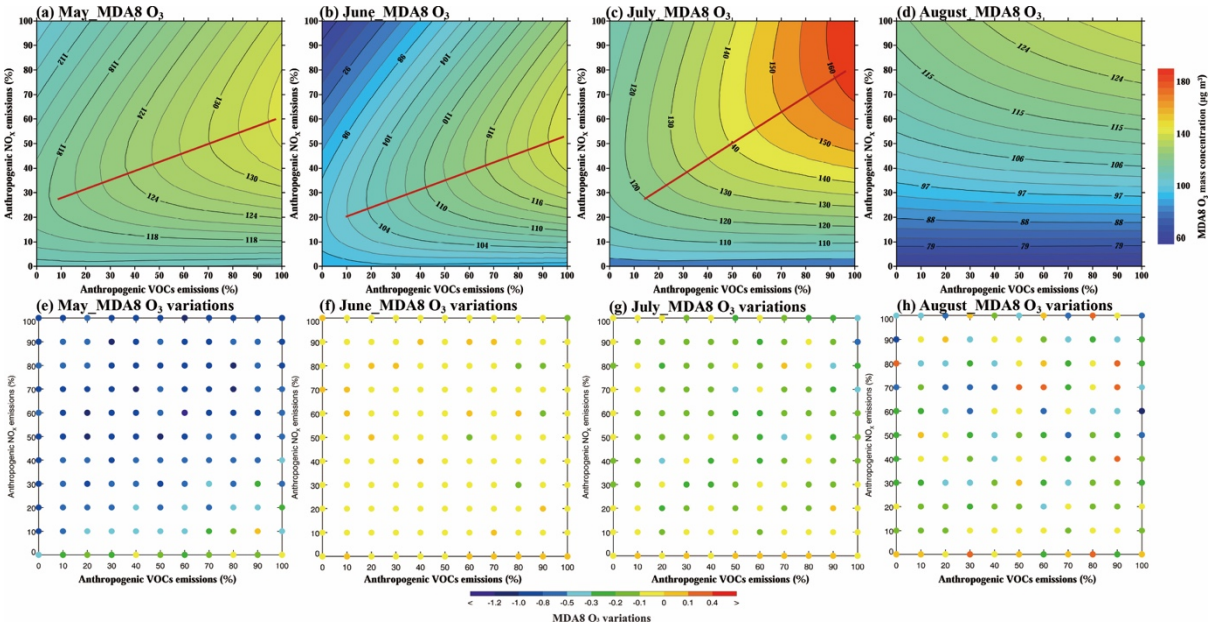

Figure S7: MDA8 O_3 isopleth profiles (μg m^{-3}) and corresponding MDA8 O_3 concentration variations in urban areas of the GZB during high-O_3 pollution episodes in 2022, with aerosol-radiation effects and heterogeneous uptake of HO_2 radicals on wet aerosol surfaces associated with aerosol variations excluded. Panels (a) and (e) show results for May, (b) and (f) for June, (c) and (g) for July, and (d) and (h) for August.